Title

Single-step metal-catalyzed synthesis of hybrid planar graphene–orbicular graphitic carbon structures using an amorphous carbon thin film as a precursor

Authors

Wang, Shengxi
Wu, Yanxia
Komvopoulos, Kyriakos

Publication Date

2021-06-01

DOI

10.1016/j.apsusc.2021.149018

Peer reviewed

Applied Surface Science 552 (2021) 149018

Contents lists available at ScienceDirect

Applied Surface Science

journal homepage: www.elsevier.com/locate/apsusc

Full Length Article

Single-step metal-catalyzed synthesis of hybrid planar graphene–orbicular graphitic carbon structures using an amorphous carbon thin film as a precursor

Shengxi Wang, Yanxia Wu [1], Kyriakos Komvopoulos [*]

Department of Mechanical Engineering, University of California, Berkeley, CA 94720, USA

ARTICLE INFO

Keywords:
Amorphous carbon
Graphene
Microstructure
Phase transformation
Thermal annealing
Thin films

ABSTRACT

Graphene is one of the strongest and most electrically and thermally conductive materials in nature; therefore, incorporating even traces of graphene into other materials can significantly enhance their mechanical, electrical, and thermal properties. Such graphene-based materials can be used in many applications, including flexible displays, batteries, supercapacitors, solar panels, and mobile devices. However, developing graphene-based 2D materials is challenging. In this study, a facile single-step synthesis method for fabricating thin layers of amorphous carbon (*a*-C) containing planar graphene (PG) and orbicular graphitic carbon (OGC) nanostructures was developed by thermal annealing in inert atmosphere using an sp^3-rich *a*-C thin film as a precursor. By annealing thin-film stacks of Si/NiFe/*a*-C, a thin layer with a hybrid *a*-C-PG-OGC structure was produced with OGC nanostructures forming on top of PG nanostructures and pyramidal $NiSi_x$ nanocrystals extending into the Si substrate due to the diffusion of nickel during elevated-temperature annealing. Raman spectroscopy and cross-sectional transmission electron microscopy confirmed the transformation from amorphous to graphitic structure in the *a*-C film during thermal annealing. The obtained results demonstrate that the development of this 2D material with a hybrid *a*-C-PG-OGC microstructure is due to a metal-catalyzed PG nucleation mechanism and a mismatch-induced OGC growth mechanism. The present method for synthesizing graphene-containing thin-film structures paves the way toward the fabrication of complex micro-assemblies where high strength and good thermoelectric properties are of paramount importance.

1. Introduction

Carbon forms allotropes characterized by different shapes and bonds associated with various hybridizations. Among different carbon allotropes, graphene and amorphous carbon (*a*-C) synthesized by physical vapor deposition (PVD) exhibit unique optical, thermal, electrical, and mechanical properties. Graphene consists of carbon atoms arranged in a hexagonal lattice, can exist as a monolayer or few layers of graphite, and exhibits extraordinary physical properties, including high conductivity, transparency, and fracture strength. Because of its unmatchable properties, graphene has been used in numerous emerging technologies, such as electronics, photonics, sensors, and membrane structures [1]. The *a*-C lacks long-range order, comprises multiple types of bonding configurations, i.e., tetrahedral (sp^3), trigonal (sp^2), and linear (sp), and its physical characteristics are principally controlled by both the dominant hybridization state and the existence of disorders, specifically the sp^2/sp^3 fraction and topological and/or structural disorders [2,3]. The combination of excellent tribomechanical properties and good thermal stability of *a*-C makes it an ideal material for applications requiring durable overcoats that can protect precious substrates from damage, mechanical wear, and corrosion, or solid lubricant layers for reducing friction traction [4–7].

Despite significant advances in *a*-C film deposition techniques, most of which utilize graphite as a precursor, the synthesis of graphene is characterized by completely dissimilar precursors (i.e., solid carbon like graphite, or carbon-containing gases like methane and acetylene) and different mechanisms. Numerous methods of graphene growth have been developed, including mechanical exfoliation and cleavage [8], anodic bonding [9], chemical exfoliation [10,11], chemical vapor deposition (CVD) [12], thermal decomposition of SiC [13], precipitation

* Corresponding author.
E-mail address: kyriakos@me.berkeley.edu (K. Komvopoulos).
[1] Present address: Institute of New Carbon Materials, Taiyuan University of Technology, Taiyuan, China.

https://doi.org/10.1016/j.apsusc.2021.149018
Received 2 October 2020; Received in revised form 2 January 2021; Accepted 9 January 2021
Available online 16 January 2021
0169-4332/

from single-crystal transition metals [14], and other less common methods [15]. Among various methods used to synthesize graphene, the transformation of non-graphitic to graphitic carbon structures has attracted significant attention because of its simplicity, low cost, and high efficiency [16–20]. In this transformation, metastable structures (e.g., *a*-C films and diamond nanoparticles) act as crystallization nuclei to instigate the growth of a graphitic structure under conditions of direct thermal annealing. However, the graphitization yield of this method is low and the extremely high annealing temperature (~3300 °C) and high pressure make it a high energy consuming process [21].

To overcome the limitations of direct thermal annealing, transition metals and alloys have been used as catalysts to enhance the growth and improve the crystallinity of graphitic structures, enabling the transformation from non-graphitic to graphitic carbon at a temperature as low as 600 °C [22]. This transformation process can be explained by the precipitation theory [23], according to which, carbon atoms diffuse into a metal layer heated at an elevated temperature and during cooling, as the solid solubility decreases, they precipitate out in the form of graphitic carbon [24,25]. However, the applicability of the precipitation theory to graphitic carbon transformation has been debated in recent years, especially after the discovery that graphitic carbon can nucleate under constant or even rising temperature conditions, which dismisses the nucleation of graphitic carbon according to the core process of the precipitation theory, i.e., cooling-induced supersaturation [26,27]. Indeed, the nucleation and growth of graphitic carbon is a surface-catalyzed process for gaseous carbon sources, such as those usually used in CVD, or a bulk diffusion process for solid carbon sources, both of which do not depend on cooling [27,28]. The current perception is that the formation of graphitic carbon in the presence of transition metals is a consequence of metal-catalyzed crystallization. The nucleation and growth of graphene in the presence of a catalytically active transition metal has been studied by in-situ transmission electron microscopy (TEM) [27]. Although the nucleation and growth of graphene have been attributed to metal catalyzation, non-equilibrium precipitation of excess carbon also occurs during cooling, resulting in inhomogeneous graphene growth [28]. This suggests that the synthesis of graphitic carbon using transition metals may be a two-step process involving metal-catalyzed crystallization followed by precipitation-induced growth.

Graphitic carbon may comprise not only planar graphene but also molecules demonstrating different morphologies. For instance, carbon nanoribbons [29], nanotubes and fullerene [30], and 3D graphitic carbon architectures [31–34] can be synthesized by manipulating basic forms of carbon and/or controlling the growth conditions. A facile, one-step process of metal-catalyzed synthesis of a hybrid microstructure consisting of orbicular graphitic carbon (OGC) grown on top of planar graphene (PG) was developed in this study. This microstructure was produced by thermal annealing, using a PVD-deposited *a*-C film as the carbon source and a film of a transition metal as the catalyst. The morphology of the grown graphitic carbon was characterized by scanning electron microscopy (SEM), high-resolution TEM, scanning TEM (STEM), and electron energy loss spectroscopy (EELS), whereas the graphitic carbon structure was examined by Raman spectroscopy and X-ray photoelectron spectroscopy (XPS). A plausible mechanism of graphene growth is proposed in the context of the obtained experimental results and observations.

2. Experimental methods

2.1. Specimen fabrication

Films of NiFe alloy with a thickness of ~20 nm were synthesized on Si(100) substrates in a radio-frequency (RF) sputter deposition apparatus (Perkin-Elmer, Randex 2400) using a hot-pressed, sintered Ni-rich (>90 wt% Ni) NiFe target with a diameter of 20 cm. The deposition conditions were 250 W RF forward power, 0.4 Pa working pressure, 30 sccm Ar flow rate, and 0.4 min deposition time. Subsequently, 17-nm-thick *a*-C films were deposited onto the NiFe-coated Si samples in a custom-made filtered cathodic vacuum arc (FCVA) system using a high purity (99.99 wt%) graphite target with a diameter of 35 mm under working conditions of ~1.3×10^{-4} Pa base pressure, ~1.5×10^{19} ions/m^2·s, and –80 V substrate bias voltage. These FCVA deposition conditions have been found to yield a uniform *a*-C film covering the entire NiFe surface [35]. Finally, the Si/NiFe/*a*-C stacks were placed in a rapid thermal annealer (AccuThermo AW610 RTP) and heated at 650 °C for 2.5 min in Ar atmosphere.

2.2. Microanalysis

Raman spectroscopy was performed with a 532-nm-wavelength laser to investigate *a*-C transformation to graphitic carbon. High-magnification SEM images obtained with an FEI Quanta 3D FEG microscope were used to identify changes in the surface morphology due to graphene formation and metal segregation during thermal annealing. XPS analysis was performed with a PHI 5400 XPS spectrometer using monochromatic Al Kα radiation. TEM and EELS studies with cross-sectional stack samples were carried out with an FEI Tecnai F20 microscope operated at 200 kV equipped with an aberration-corrected condenser and a Gatan imaging filter. Both the untreated and annealed cross-sectional stacks were coated with a Cr capping layer by ion-beam deposition and were then glued face-to-face using epoxy bond. The cross-sectional TEM samples were prepared by a wedge polishing method detailed elsewhere [36]. For the analysis of the Raman, XPS, and EELS spectra, multiple measurements were obtained from three different locations of each sample to ensure the repeatability of the results.

3. Results and discussion

Fig. 1(a) shows Raman spectra of *a*-C films obtained before and after thermal annealing that confirm the formation of graphitic carbon. The Raman spectrum of the as-grown *a*-C film exhibits a broad peak in the range of 1100–1800 cm^{-1}, which is indicative of the formation of *a*-C. The spectrum was fitted with two Gaussian distributions assigned to D and G peaks centered at 1409 and 1579 cm^{-1}, respectively [Fig. 1(b), top spectrum]. The relatively low intensity of the D peak indicates the presence of few disordered sp^2 clusters in the as-grown film, which is a characteristic feature of sp^3-rich *a*-C films [3,37]. A comparison of the Raman spectrum of the as-grown *a*-C film with those of *a*-C films deposited under similar conditions using the same FCVA system [38] confirmed that the as-grown *a*-C film was rich in sp^3 hybridized carbon, in agreement with sp^3 estimates derived from EELS measurements [35]. The sharp apex of the G peak may be attributed to isolated sp^2-bonded defects in the extended sp^3 matrix [39]. The Raman spectrum of the same *a*-C film obtained after thermal annealing [Fig. 1(a)] comprises four distinct peaks that were fitted with Lorentzian distributions. These peaks are referred to as the D (1362 cm^{-1}), G (1589 cm^{-1}), 2D (2696 cm^{-1}), and D + D′ (~2950 cm^{-1}) peaks [Fig. 1(b), bottom spectrum]. The G and 2D peaks are characteristic of graphene. Because Raman spectroscopy is sensitive to sp^2 hybridization, the higher intensity and upward shift of the G peak in the Raman spectrum of the thermally annealed *a*-C film imply a carbon structure with increased sp^2 hybridization. This is evidence for the transformation from sp^3-rich *a*-C to graphitic carbon. The D peak is usually attributed to broken crystal symmetry and illuminates the existence of defects or grain boundaries in

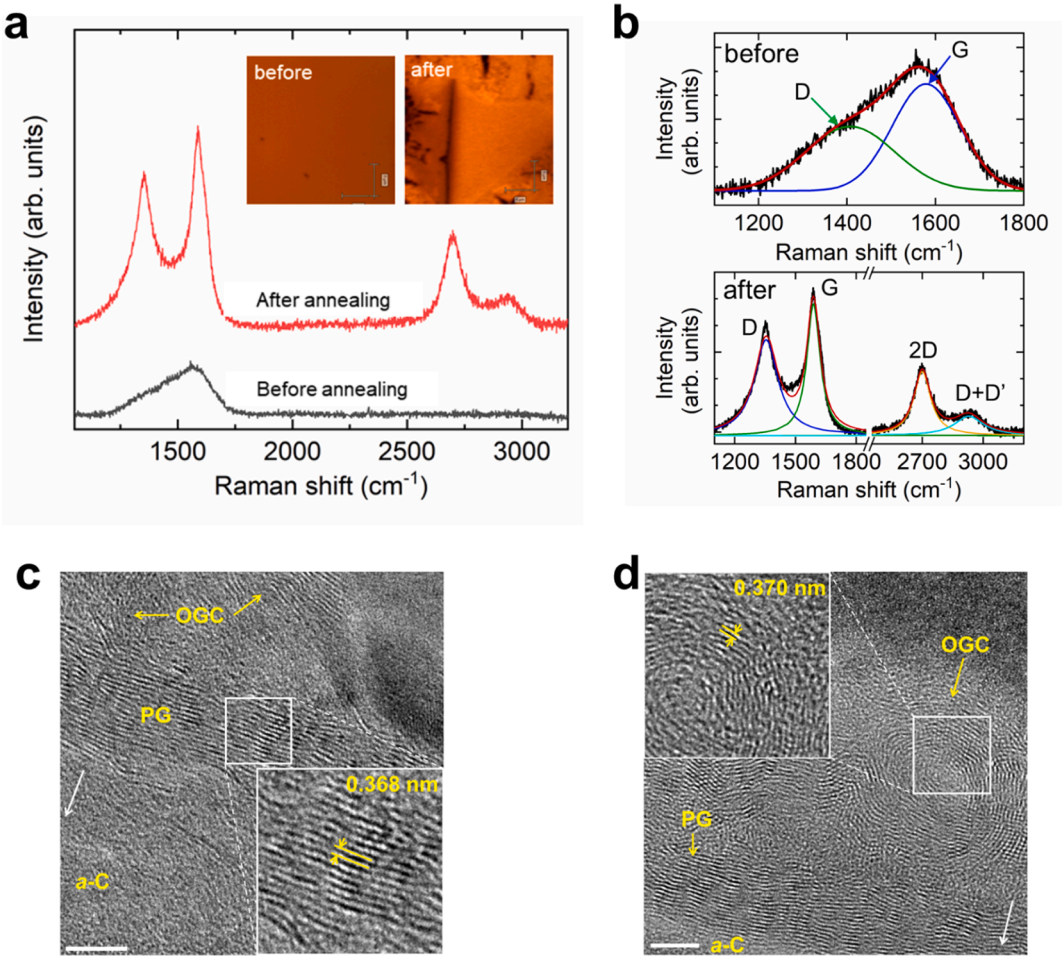

Fig. 1. (a) Raman spectra of an *a*-C film obtained before and after thermal annealing at 650 °C in Ar atmosphere. (b) The D (~1350 cm^{-1}) and G (~1580 cm^{-1}) peaks in the spectrum of the *a*-C film obtained before annealing were fitted with Gaussian distributions, whereas the D (~1350 cm^{-1}), G (~1580 cm^{-1}), 2D (~2680 cm^{-1}), and D + D′ (~2950 cm^{-1}) peaks in the spectrum of the *a*-C film obtained after annealing were fitted with Lorentzian distributions. (c) & (d) Cross-sectional TEM images of thermally annealed Si/NiFe/*a*-C/Cr sample stacks revealing the formation of planar graphene (PG) and orbicular graphitic carbon (OGC) nanostructures. The magnified boxed insets show the measured spacing of the graphitic layers in the PG and OGC nanostructures. The white arrow in the TEM images points to the direction of the Si susbtrate. The scale bars are equal to 5 nm.

the graphitic crystalline regions. The 2D peak is the second-order overtone of the D peak, may exist even in the absence of defects, and is considered to be a fingerprint of a graphitic structure. The D + D′ peak is a combination of two vibrational modes of different momentum and its presence is also associated with defects in the graphitic structure [40].

The TEM images shown in Fig. 1(c) and (d) reveal that thermal annealing led to the formation of a hybrid film microstructure consisting of planar graphene (PG), orbicular graphitic carbon (OGC), and residual *a*-C. In particular, Fig. 1(c) shows that PG comprised ~18 graphitic planes with a lamellar spacing of 0.368 nm, which matches that of a layered graphene structure, and residual *a*-C underneath it. The in-plane size of PG was found to be several hundred nanometers [Fig. 2(a)]. Figs. 1(c) and 2(a) show that some of the amorphous carbon did not transform to graphitic carbon, implying partial *a*-C to graphene transformation. The TEM image shown in Fig. 1(d) reveals the formation of OGC over the PG, remote from the Si substrate. The inset of Fig. 1(d) shows that the lamellar spacing of the OGC is 0.370 nm. More evidence of PG growth on top of residual *a*-C and the formation of OGC above the PG is provided in the TEM images shown Fig. 2(b).

Fig. 3 shows the deconvolution of the XPS C1s core-level spectrum of thermally annealed *a*-C film that comprises a carbon peak centered at ~284.4 eV with four Gaussian distributions, namely sp^2 C (graphitic carbon) at 284.4 eV, sp^3 C (diamondlike carbon) at 285.6 eV, C–O at 286.6 eV, and O–C=O at 288.5 eV. The profoundly higher intensity of the sp^2 peak indicates that thermal annealing led to the formation of a graphitic microstructure with an estimated sp^2 content (obtained as the $sp^2/(sp^2 + sp^3)$ area fraction) equal to ~87.6%. The small sp^3 peak is attributed to diamondlike carbon embedded in residual *a*-C and the existence of sp^3 type defects in the graphitic carbon [41,42]. The minor C–O and O–C=O peaks indicate partial oxidation, which is attributed to the sample exposure to the atmosphere during handling and transferring from the thermal annealer to the XPS. Therefore, the XPS analysis yields further confirmation about the graphitization of the as-grown sp^3-rich *a*-C film during thermal annealing.

The surface morphology of the sample provides additional insight into graphitization and the role of the NiFe catalyst during thermal annealing. The smooth surface shown in Fig. 4(a) indicates a uniform coverage of the NiFe underlayer by the deposited *a*-C film. However, after thermal annealing the surface morphology exhibited roughening

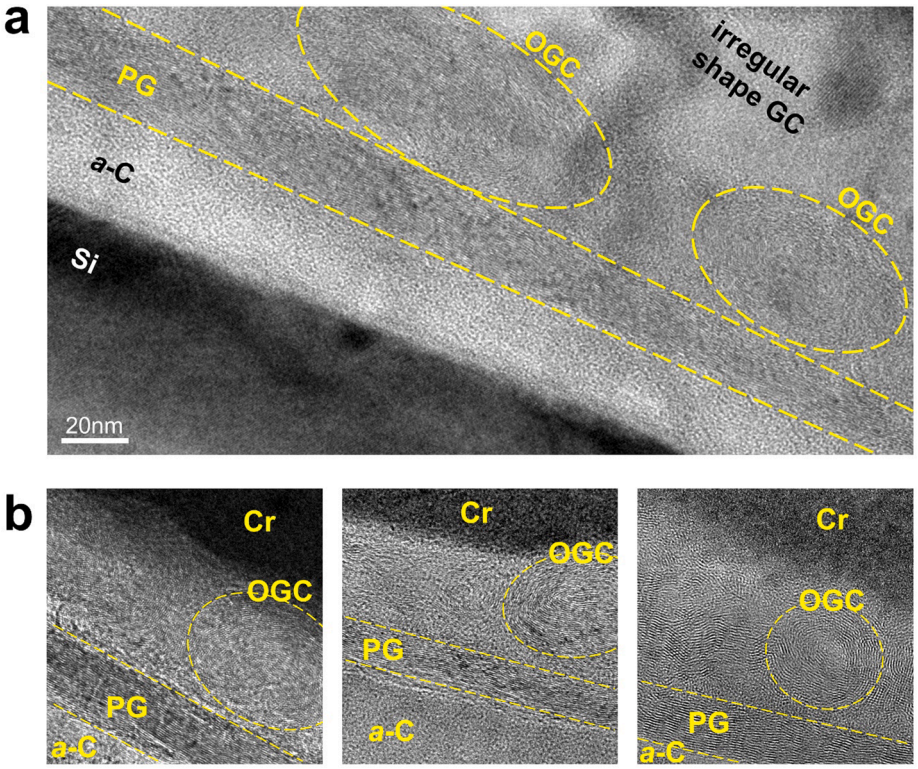

Fig. 2. (a) Cross-sectional TEM image of a thermally annealed Si/NiFe/*a*-C/Cr sample stack revealing the formation of orbicular graphitic carbon (OGC) on top of planar graphene (PG) in the bulk of the *a*-C film capped by irregular shape graphitic carbon (GC) and (b) high-magnification TEM images showing OGC formation on top of PG in the bulk of the *a*-C film.

and dark islands surrounded by large bright areas [Fig. 4(b)]. These changes in the surface morphology are attributed to NiFe agglomeration and Ostwald ripening, while the effect of the *a*-C film on metal agglomeration is believed to be secondary [27,43]. Fig. 4(c) shows high-magnification SEM images of the boxed area shown in Fig. 4(b), revealing a worm-like morphology for the bright area (A) and a textured morphology for the dark area (B) possessing tiny dark spots. From the carbon and metal characteristics observed under high-resolution SEM, it may be inferred that the dark and bright spots in area B are regions containing only carbon and metal agglomerates covered by carbon, respectively. The cross-sectional TEM images of the Si/NiFe/*a*-C/Cr sample stacks obtained after thermal annealing [Fig. 4(d)–(f)] provide evidence for the aforementioned structure changes responsible for the morphology characteristics seen in Fig. 4(b) and (c). Specifically, three cross-sectional structures characterize the annealed sample, i.e., pure carbon [Fig. 4(d)], carbon-covered NiFe [Fig. 4(e)], and pure NiFe agglomerate [Fig. 4(i)].

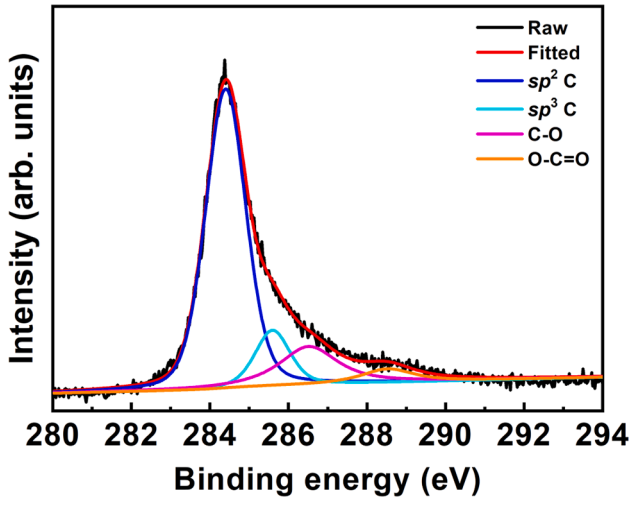

Fig. 3. Deconvolution of the XPS C1s spectrum of an *a*-C film that was thermally annealed at 650 °C in Ar atmosphere with four fitted Gaussian distributions assigned to sp^2 C, sp^3 C, C–O, and O–C=O.

Raman spectroscopy produced additional evidence of *a*-C transformation to graphitic carbon, while cross-sectional TEM images yielded direct proof for the formation of PG and OGC in the thermally annealed *a*-C film. Insight into the role of the NiFe underlayer during the thermal annealing process is critical to understanding this transformation process. The cross-sectional TEM images obtained after thermal annealing [Figs. 1(c), 1(d), 2(a), and 4(d)] show the *a*-C film in direct contact with the Si substrate. Such crystallization of an amorphous structure may be explained by the metal-induced layer exchange (MILE) theory. According to this theory, an amorphous film may exchange positions with a metal catalyst residing either on top or under the film, inducing amorphous-to-crystalline transformation in the film structure [44,45]. However, such layer exchange was not observed in the present study because no NiFe was found on top of the residual *a*-C or the graphene structures. Graphene growth parallel to the *a*-C/Ni interface has been attributed to an atomic level coherent match between metal and graphitic carbon [46]. However, the formation of PG in the *a*-C film remotely from the original *a*-C/NiFe interface [Figs. 4(d) and 2(a)] does not support the foregoing assertion. The rapid transformation process observed in the present study (e.g., ~18 layers of graphene formed within only 0.5 min of thermal annealing) does not support the relatively slow transformation in the MILE process due to the low carbon solubility in transition metals, where the formation of a similar number of graphene layers is typically encountered after thermal annealing for 10–60 min at a higher temperature [44,46].

Fig. 5 shows cross-sectional TEM images and elemental maps of annealed Si/NiFe/*a*-C/Cr sample stacks elucidating the role of the NiFe

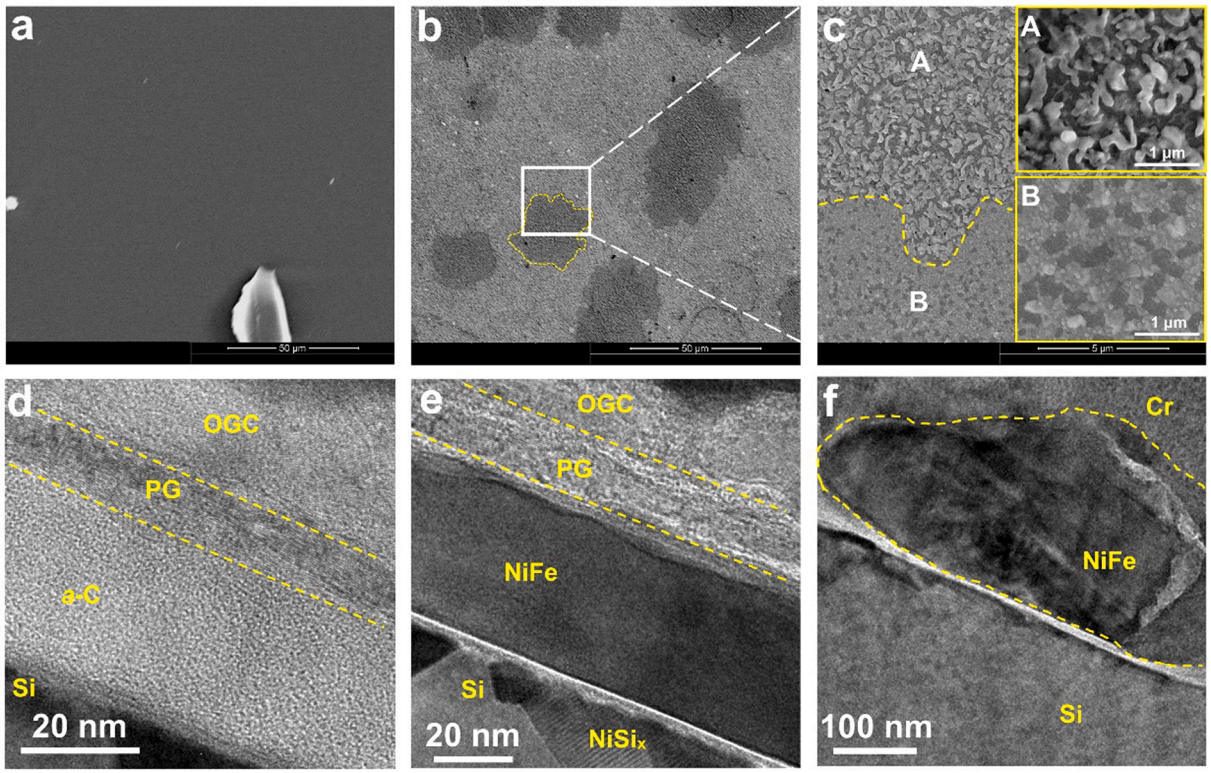

Fig. 4. SEM images of the surface morphology of an *a*-C film obtained (a) before thermal annealing (the small particles are contaminats from sample handling) and (b) after thermal annealing at 650 °C for 2.5 min in Ar atmosphere. (c) High-magnification images of two distinctly different regions A and B of the boxed region shown in (b). (d)–(f) Cross-sectional TEM images of Si/NiFe/*a*-C/Cr sample stacks obtained after thermal annealing at 650 °C for 2.5 min in Ar atmosphere showing (d) PG and OGC formation at the surface of the *a*-C film and (e) at the top of a NiFe agglomerate, and (f) a NiFe agglomerate in contact with the Si substrate produced from metal segregation.

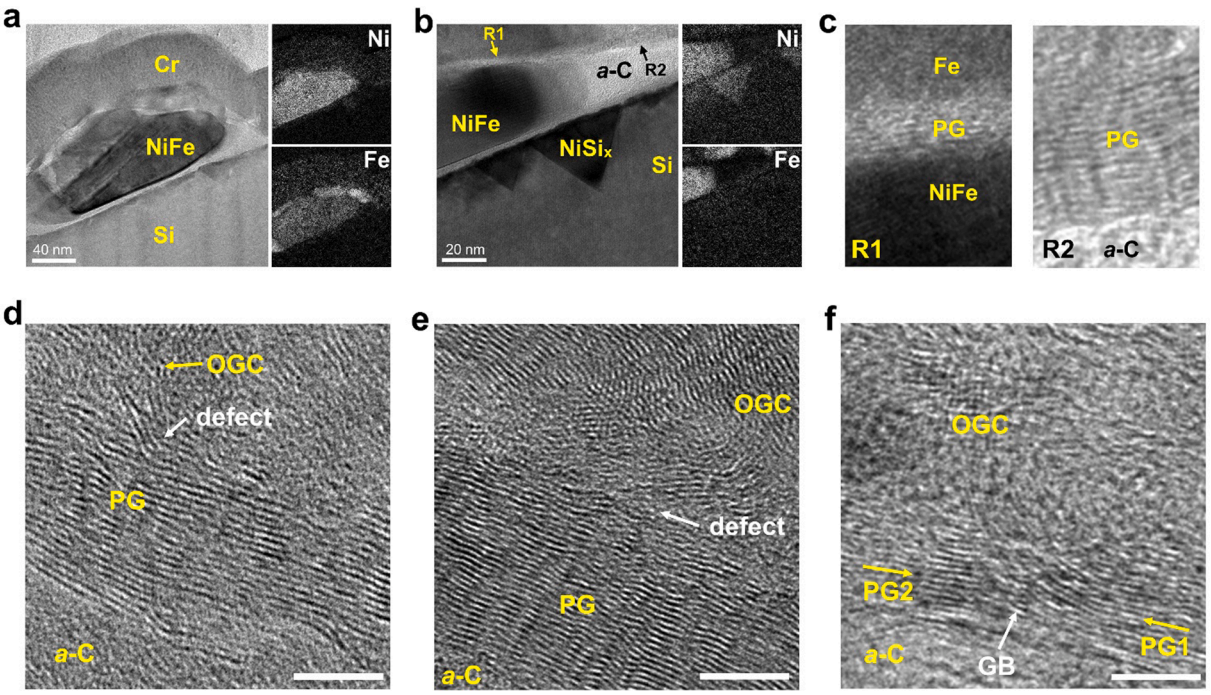

Fig. 5. Cross-sectional TEM images and elemental maps of Si/NiFe/*a*-C/Cr sample stacks obtained after thermal annealing at 650 °C for 2.5 min in Ar atmosphere revealing (a) NiFe agglomeration at the surface of the Si substrate and (b) graphene formation on top of a NiFe agglomerate and at the surface of the *a*-C film. (c) High-magnification TEM images of two regions marked as R1 and R2 in (b) illustrating the formation of graphene on top of a NiFe agglomerate (R1 region) and at the surface of the *a*-C film (R2 region). (d)–(f) Formation of OGC from defects or a grain boundary (GB) of PG nanostructures. The two yellow arrows in (f) point toward the GB of the PG1 and PG2 nanostructures. All scale bars in (d)–(f) are equal to 5 nm. (For interpretation of the references to colour in this figure legend, the reader is referred to the web version of this article.)

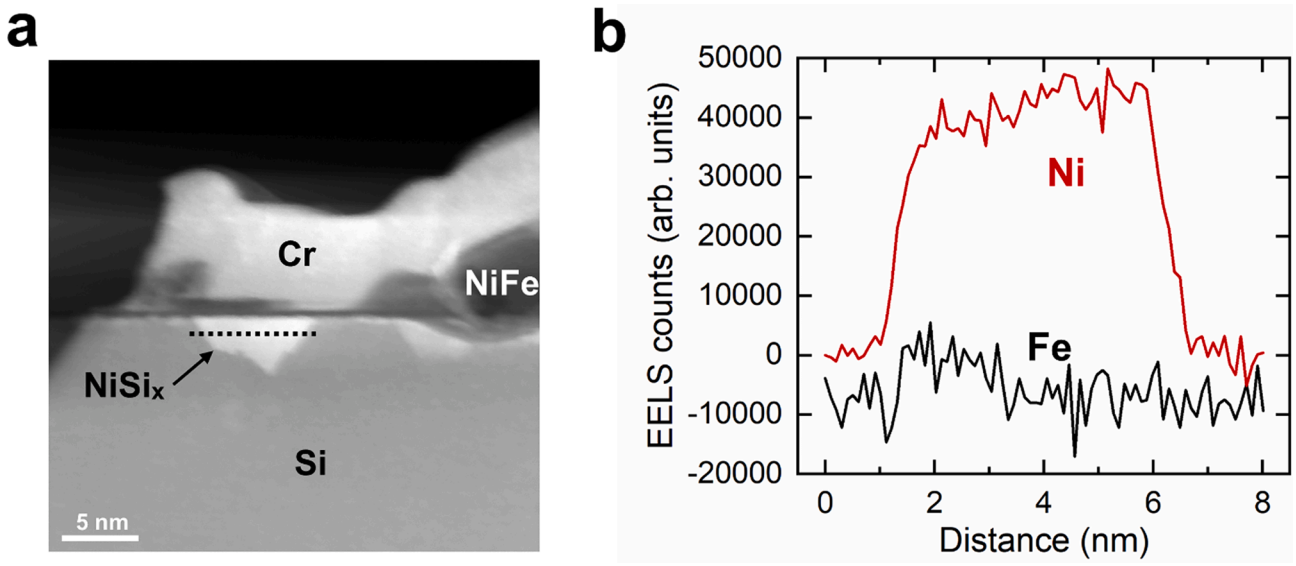

Fig. 6. (a) Cross-sectional STEM image of a Si/NiFe/*a*-C/Cr sample stack thermally annealed at 650 °C in Ar atmosphere (the dashed line indicates the scan path) and (b) EELS intensity of Ni and Fe along the scan path. The high Ni intensity and the negligible Fe intensity suggest that the composition of the pyramidal nanostructure grown into the Si substrate is nickel silicide ($NiSi_x$).

underlayer and the formation of PG and OGC in the *a*-C film. Thermal annealing disrupted the continuity of the FeNi underlayer, resulting in the formation of metal agglomerates much thicker than its thickness [Fig. 5(a)]. Elemental maps indicated that segregation produced Ni-rich agglomerates encased by an Fe-rich surface layer [insets of Fig. 5(a)]. The retraction of the NiFe underlayer explains the direct contact of the residual *a*-C film with the Si substrate [Figs. 4(d) and 2(a)]. An inspection of the boundary between a metal agglomerate and residual *a*-C [Fig. 5(b)] suggests that the NiFe underlayer played a dual role, revealed by the formation of Ni-rich agglomerates on top of the Si substrate and the growth of crystalline metal silicide into the Si substrate (the black pyramidal structures shown in Fig. 4(b)). Elemental mapping showed that the metal agglomerates consisted of Ni and Fe and that the metal silicide was $NiSi_x$. Further evidence of the growth of pyramidal $NiSi_x$ nanostructures into the surface of the Si substrate was obtained from STEM/EELS analysis [Fig. 6]. The formation of $NiSi_x$ at the Ni/Si interface as a result of thermal annealing is consistent with previous findings [47]. The TEM analysis of this study also revealed the preferential growth of $NiSi_x$ at the NiFe/Si interface. High-resolution TEM of the bright region R1 confirmed the conformal formation of PG on top of the NiFe agglomerate [Fig. 1(c)], validating the nucleation of PG at the NiFe/*a*-C boundary. The foregoing was followed by graphene growth from the nucleation site parallel to the *a*-C film surface, resulting in PG formation in region R2 [Fig. 5(b) and (c)] similar to graphene growth on top of the residual *a*-C. The TEM analysis also showed that the formation of OGC was due to a mismatch-induced growth mechanism. Indeed, graphitic layers were observed to grow away from the PG surface at defect locations or grain boundaries, forming closely packed rolled graphene layers [Fig. 5(d)–(f)], which is the energetically favorable configuration [48]. The high intensity of the D and D + D′ peaks in the Raman spectrum of the annealed sample [Fig. 1(b)] prove the presence of defects and grain boundaries in the grown graphene that acted as mismatch sites of OGC nucleation. In addition to the mismatch-induced growth mechanism of OGC, metal contamination of the PG structure and metal particles at the PG surface produced by NiFe segregation may also contribute to the formation of OGC. The presence of Fe particles at the PG surface was confirmed by elemental mapping [e.g., region R1 in Fig. 5(b) and (c)]. Detecting the effects of the carbon solubilities in Ni and Fe and the uncontrollable metal segregation on the orientation of graphene is challenging and requires further investigation.

In the light of the obtained results, the growth mechanisms of PG and OGC in thermally annealed *a*-C films can be schematically illustrated as shown in Fig. 7. Segregation of the NiFe underlayer during thermal annealing led to the formation of NiFe agglomerates, resulting in direct contact of the residual *a*-C with the Si substrate. Subsequent nucleation of PG on top of the NiFe agglomerates and OGC from defect sites and grain boundaries in the PG produced a hybrid PG-OGC microstructure, which can be potentially used to fabricate novel 3D micro-assemblies by stacking and folding. In addition, the incorporation of $NiSi_x$ in graphene makes the resulting structure compatible with electronic nanodevices, hence showing a potential of the $NiSi_x$/graphene hybrid microstructure for widespread applications [49].

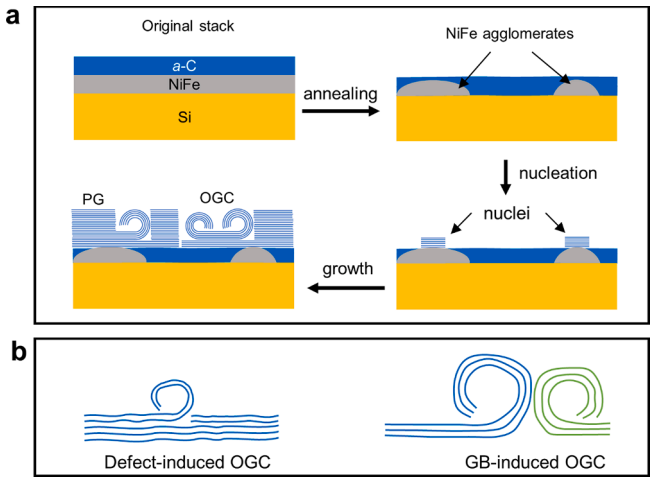

Fig. 7. Schematic illustration of the mechanisms controlling the growth of planar graphene (PG) and orbicular graphitic carbon (OGC) by thermal annealing at 650 °C in Ar atmosphere: (a) NiFe agglomeration, PG nucleation on NiFe agglomerates, PG growth on top of NiFe agglomerates and *a*-C film, and OGC growth from mismatch-induced growth sites, i.e., defects and grain boundaries (GB), in the PG, yielding a hybrid PG-OGC microstructure and (b) mismatch-induced OGC growth from a PG defect or the GB of two PG nanostructures.

4. Conclusions

A one-step process for synthesizing hybrid PG and OGC nanostructures using NiFe-catalyzed transformation of *a*-C thin films was developed in this study. Raman and XPS results confirmed the transformation of *a*-C to graphene during thermal annealing. Cross-sectional TEM and elemental mapping revealed the formation of NiFe agglomerates at the surface of the Si substrate as a result of metal migration and Ostwald ripening. The produced graphitic carbon was found to comprise PG and OGC on top of the PG. SEM and cross-sectional TEM showed that the formation of PG can be attributed to graphene nucleation from NiFe agglomerates and graphene growth along the surface of the *a*-C film. The segregation of NiFe resulted in the uncontrollable growth of OGC that nucleated at mismatch-induced growth sites in the PG nanostructure. Elemental mapping and STEM/EELS analysis revealed the growth of pyramidal $NiSi_x$ nanostructures into the surface of the Si substrate. The synthesized hybrid PG-OGC microstructure with pyramidal $NiSi_x$ nanocrystals extending into the Si substrate presents an interesting prospect for nanoelectronic applications.

Declaration of Competing Interest

The authors declare that they have no known competing financial interests or personal relationships that could have appeared to influence the work reported in this paper.

Acknowledgements

This research was partially funded by Western Digital Technologies, Inc. The TEM/EELS studies were carried out at the National Center for Electron Microscopy, Molecular Foundry, Lawrence Berkeley National Laboratory. The work at the Molecular Foundry was supported by the Office of Science, Office of Basic Energy Sciences, of the U.S. Department of Energy under Contract No. DE-AC02-05CH11231.

Author contribution

S.W. and Y.W. performed all of the experiments and wrote the first draft of the paper. K.K. defined the scope of the entire work, supervised the research of S.W. and Y.W., examined the results, and wrote the final manuscript of the paper.

References

[1] Y. Zhu, S. Murali, W. Cai, X. Li, J.W. Suk, J.R. Potts, R.S. Ruoff, Graphene and graphene oxide: synthesis, properties, and applications, Adv. Mater. 22 (2010) 3906–3924.
[2] S. Wang, K. Komvopoulos, Structure evolution during deposition and thermal annealing of amorphous carbon ultrathin films investigated by molecular dynamics simulations, Sci. Rep. 10 (2020) 8089.
[3] J. Robertson, Diamond-like amorphous carbon, Mater. Sci. Eng. R: Rep. 37 (2002) 129–281.
[4] G.W. Malaczynski, A.H. Hamdi, A.A. Elmoursi, X. Qiu, Diamond-like carbon coating for aluminum 390 alloy – automotive applications, Surf. Coat. Technol. 93 (1997) 280–286.
[5] A.A. Voevodin, J.P. O'Neill, J.S. Zabinski, Nanocomposite tribological coatings for aerospace applications, Surf. Coat. Technol. 116 (1999) 36–45.
[6] J. Matlak, E. Rismaniyazdi, K. Komvopoulos, Nanostructure, structural stability, and diffusion characteristics of layered coatings for heat-assisted magnetic recording head media, Sci. Rep. 8 (2018) 9807.
[7] D. Berman, B. Narayanan, M.J. Cherukara, S.K.R.S. Sankaranarayanan, A. Erdemir, A. Zinovev, A.V. Sumant, *Operando* tribochemical formation of onion-like carbon leads to macroscale superlubricity, Nat. Commun. 9 (2018) 1164.
[8] K.S. Novoselov, D. Jiang, F. Schedin, T.J. Booth, V.V. Khotkevich, S.V. Morozov, A. K. Geim, Two-dimensional atomic crystals, Proc. Natl. Acad. Sci. USA 102 (2005) 10451–10453.
[9] T. Moldt, A. Eckmann, P. Klar, S.V. Morozov, A.A. Zhukov, K.S. Novoselov, C. Casiraghi, High-yield production and transfer of graphene flakes obtained by anodic bonding, ACS Nano 5 (2011) 7700–7706.
[10] S. Stankovich, D.A. Dikin, R.D. Piner, K.A. Kohlhaas, A. Kleinhammes, Y. Jia, Y. Wu, S.T. Nguyen, R.S. Ruoff, Synthesis of graphene-based nanosheets via chemical reduction of exfoliated graphite oxide, Carbon 45 (2007) 1558–1565.
[11] Y. Hernandez, V. Nicolosi, M. Lotya, F.M. Blighe, Z. Sun, S. De, I.T. Mcgovern, B. Holland, M. Byrne, Y.K. Gun'ko, J.J. Boland, P. Niraj, G. Duesberg, S. Krishnamurthy, R. Goodhue, J. Hutchison, V. Scardaci, A.C. Ferrari, J. N. Coleman, High-yield production of graphene by liquid-phase exfoliation of graphite, Nat. Nanotechnol. 3 (2008) 563–568.
[12] A. Reina, X. Jia, J. Ho, D. Nezich, H. Son, V. Bulovic, M.S. Dresselhaus, J. Kong, Large area, few-layer graphene films on arbitrary substrates by chemical vapor deposition, Nano Lett. 9 (2009) 30–35.
[13] Y.Q. Wu, P.D. Ye, M.A. Capano, Y. Xuan, Y. Sui, M. Qi, J.A. Cooper, T. Shen, D. Pandey, G. Prakash, R. Reifenberger, Top-gated graphene field-effect-transistors formed by decomposition of SiC, Appl. Phys. Lett. 92 (2008) 092102.
[14] W. Choi, I. Lahiri, R. Seelaboyina, Y.S. Kang, Synthesis of graphene and its applications: a review, Crit. Rev. Solid State Mater. Sci. 35 (2010) 52–71.
[15] S.A. Bhuyan, N. Uddin, M. Islam, F.A. Bipasha, S.S. Hossain, Synthesis of graphene, Intl. Nano Lett. 6 (2016) 65–83.
[16] C. Maddi, F. Bourquard, V. Barnier, J. Avila, M.-C. Asensio, T. Tite, C. Donnet, F. Garrelie, Nano-architecture of nitrogen-doped graphene films synthesized from a solid CN source, Sci. Rep. 8 (2018) 3247.
[17] M. Zheng, K. Takei, B. Hsia, H. Fang, X. Zhang, N. Ferralis, H. Ko, Y.-L. Chueh, Y. Zhang, R. Maboudian, A. Javey, Metal-catalyzed crystallization of amorphous carbon to graphene, Appl. Phys. Lett. 96 (2010) 063110.
[18] Y. Chen, J. Wang, P. Schützendübe, Z. Wang, E.J. Mittemeijer, Very low-temperature growth of few-layer graphene by Ni-induced crystallization of amorphous carbon in vacuum, Carbon 159 (2020) 37–44.
[19] A.T.T. Koh, Y.M. Foong, D.H.C. Chua, Comparison of the mechanism of low defect few-layer graphene fabricated on different metals by pulsed laser deposit, Diamond Relat. Mater. 25 (2012) 98–102.
[20] A. Barreiro, F. Börrnert, S.M. Avdoshenko, B. Rellinghaus, G. Cuniberti, M. H. Rümmeli, L.M.K. Vandersypen, Understanding the catalyst-free transformation of amorphous carbon into graphene by current-induced annealing, Sci. Rep. 3 (2013) 1115.
[21] J. Peng, N. Chen, R. He, Z. Wang, S. Dai, X. Jin, Electrochemically driven transformation of amorphous carbons to crystalline graphite nanoflakes: a facile and mild graphitization method, Angew. Chem. 129 (2017) 1777–1781.
[22] Y. Wu, S. Wang, K. Komvopoulos, A review of graphene synthesis by indirect and direct deposition methods, J. Mater. Res. 35 (2020) 76–89.
[23] M. Eizenberg, J.M. Blakely, Carbon monolayer phase condensation on Ni(111), Surf. Sci. 82 (1979) 228–236.
[24] J.M. García, R. He, M.P. Jiang, P. Kim, L.N. Pfeiffer, A. Pinczuk, Multilayer graphene grown by precipitation upon cooling of nickel on diamond, Carbon 49 (2011) 1006–1012.
[25] D. Berman, S.A. Deshmukh, B. Narayanan, S.K.R.S. Sankaranarayanan, Z. Yan, A. A. Balandin, A. Zinovev, D. Rosenmann, A.V. Sumant, Metal-induced rapid transformation of diamond into single and multilayer graphene on wafer scale, Nat. Commun. 7 (2016) 12099.
[26] K.L. Saenger, J.C. Tsang, A.A. Bol, J.O. Chu, A. Grill, C. Lavoie, *In situ* x-ray diffraction study of graphitic carbon formed during heating and cooling of amorphous-C/Ni bilayers, Appl. Phys. Lett. 96 (2010) 153105.
[27] J.A. Rodríguez-Manzo, C. Pham-Huu, F. Banhart, Graphene growth by a metal-catalyzed solid-state transformation of amorphous carbon, ACS Nano 5 (2011) 1529–1534.
[28] X. Li, W. Cai, J. An, S. Kim, J. Nah, D. Yang, R. Piner, A. Velamakanni, I. Jung, E. Tutuc, S.K. Banerjee, L. Colombo, R.S. Ruoff, Large-area synthesis of high-quality and uniform graphene films on copper foils, Science 324 (2009) 1312–1314.
[29] L. Jiao, L. Zhang, X. Wang, G. Diankov, H. Dai, Narrow graphene nanoribbons from carbon nanotubes, Nature 458 (2009) 877–880.
[30] A.K. Geim, K.S. Novoselov, The rise of graphene, in: P. Rodgers (Ed.), Nanoscience and Technology, Nature Publishing Group, 2009, pp. 11–19.
[31] H. Chen, X.-L. Zhang, Y.-Y. Zhang, D. Wang, D.-L. Bao, Y. Que, W. Xiao, S. Du, M. Ouyang, S.T. Pantelides, H.-J. Gao, Atomically-precise, custom-design origami graphene nanostructures, Science 365 (2019) 1036–1040.
[32] K. Li, G. Eres, J. Howe, Y.-J. Chuang, X. Li, Z. Gu, L. Zhang, S. Xie, Z. Pan, Self-assembly of graphene on carbon nanotube surfaces, Sci. Rep. 3 (2013) 2353.
[33] A.G. Nasibulin, P.V. Pikhitsa, H. Jiang, D.P. Brown, A.V. Krasheninnikov, A. S. Anisimov, P. Queipo, A. Moisala, D. Gonzalez, G. Lientschnig, A. Hassanien, S. D. Shandakov, G. Lolli, D.E. Resasco, M. Choi, D. Tománek, E.I. Kauppinen, A novel hybrid carbon material, Nat. Nanotechnol. 2 (2007) 156–161.
[34] R.K. Paul, M. Ghazinejad, M. Penchev, J. Lin, M. Ozkan, C.S. Ozkan, Synthesis of a pillared graphene nanostructure: a counterpart of three-dimensional carbon architectures, Small 6 (2010) 2309–2313.
[35] J. Matlak, K. Komvopoulos, Ultrathin amorphous carbon films synthesized by filtered cathodic vacuum arc used as protective overcoats of heat-assisted magnetic recording heads, Sci. Rep. 8 (2018) 9647.
[36] P.M. Voyles, J.L. Grazul, D.A. Muller, Imaging individual atoms inside crystals with ADF-STEM, Ultramicroscopy 96 (2003) 251–273.
[37] D.G. McCulloch, S. Prawer, A. Hoffman, Structural investigation of xenon-ion-beam-irradiated glassy carbon, Phys. Rev. B 50 (1994) 5905–5917.
[38] J. Xie, K. Komvopoulos, The role of duty cycle of substrate pulse biasing in filtered cathodic vacuum arc deposition of amorphous carbon films, IEEE Trans. Magn. 51 (2015) 3302009.
[39] S. Prawer, K.W. Nugent, Y. Lifshitz, G.D. Lempert, E. Grossman, J. Kulik, I. Avigal, R. Kalish, Systematic variation of the Raman spectra of DLC films as a function of sp^2:sp^3 composition, Diamond Relat. Mater. 5 (1996) 433–438.
[40] R. Saito, M. Hofmann, G. Dresselhaus, A. Jorio, M.S. Dresselhaus, Raman spectroscopy of graphene and carbon nanotubes, Adv. Phys. 60 (2011) 413–550.

[41] S. Park, J. An, J.R. Potts, A. Velamakanni, S. Murali, R.S. Ruoff, Hydrazine-reduction of graphite- and graphene oxide, Carbon 49 (2011) 3019–3023.
[42] A. Siokou, F. Ravani, S. Karakalos, O. Frank, M. Kalbac, C. Galiotis, Surface refinement and electronic properties of graphene layers grown on copper substrate: an XPS, UPS and EELS study, Appl. Surf. Sci. 257 (2011) 9785–9790.
[43] M. Miyoshi, M. Mizuno, K. Banno, T. Kubo, T. Egawa, T. Soga, Study on transfer-free graphene synthesis process utilizing spontaneous agglomeration of catalytic Ni and Co metals, Mater. Res. Express 2 (2015) 015602.
[44] H. Murata, K. Toko, N. Saitoh, N. Yoshizawa, T. Suemasu, Direct synthesis of multilayer graphene on an insulator by Ni-induced layer exchange growth of amorphous carbon, Appl. Phys. Lett. 110 (2017) 033108.
[45] J.Y. Wang, Z.M. Wang, E.J. Mittemeijer, Mechanism of aluminum-induced layer exchange upon low-temperature annealing of amorphous Si/polycrystalline Al bilayers, J. Appl. Phys. 102 (2007) 113523.
[46] H. Li, X. Li, J. Wei, Z. Wang, P. Guo, P. Ke, H. Saito, P. Cui, A. Wang, Crystalline transformation from ta-C to graphene induced by a catalytic Ni layer during annealing, Diamond Relat. Mater. 101 (2020) 107556.
[47] T. Tite, V. Barnier, C. Donnet, A.-S. Loir, S. Reynaud, J.-Y. Michalon, F. Vocanson, F. Garrelie, Surface enhanced Raman spectroscopy platform based on graphene with one-year stability, Thin Solid Films 604 (2016) 74–80.
[48] R. Wenisch, R. Hübner, F. Munnik, S. Melkhanova, S. Gemming, G. Abrasonis, M. Krause, Nickel-enhanced graphitic ordering of carbon ad-atoms during physical vapor deposition, Carbon 100 (2016) 656–663.
[49] O. Vilkov, A. Fedorov, D. Usachov, L.V. Yashina, A.V. Generalov, K. Borygina, N. I. Verbitskiy, A. Grüneis, D.V. Vyalikh, Controlled assembly of graphene-capped nickel, cobalt and iron silicides, Sci. Rep. 3 (2013) 2168.